Energy Conversion and Management 299 (2024) 117877

Contents lists available at ScienceDirect

Energy Conversion and Management

journal homepage: www.elsevier.com/locate/enconman

Determination and validation of polarization losses parameters to predict current/voltage-characteristics for SOFC button cell

Luca Del Zotto [a], Giacomo Tamburrano [b], Alessandro Dell'Era [c,*], Arda Hatunoglu [d], Erwin Ciro [b]

[a] CREAT Centro di Ricerca su Energia, Ambiente e Territorio, Università Telematica eCampus, 22060 Novedrate, Italy
[b] Department of Engineering Sciences, Università degli Studi Guglielmo Marconi, 00193 Rome, Italy
[c] Department of Basic and Applied Science for Engineering, Sapienza University of Rome, 00161 Rome, Italy
[d] Department of Astronautics, Electrical and Energy Engineering, Sapienza Università di Roma, Via Eudossiana 18, 00184 Rome, Italy

ARTICLE INFO

Keywords:
Solid oxide fuel cell
Modeling
Electrochemical impedance spectroscopy
Distribution of relaxation times
Reaction mechanisms

ABSTRACT

Solid Oxide Fuel Cell represents a valid and clean alternative to conventional combined heat and power systems. These devices can convert different kinds of fuels into electricity with high efficiencies (up to 75–80 %) and low CO_2 or hazardous emissions. In order to understand and validate Solid Oxide Fuel Cell behavior at different operating conditions, investigations are currently focusing their attention on modeling. In this work, an experimental-based model to study the effect of different hydrogen and temperature conditions on both the polarization processes and its effect on Solid Oxide Fuel Cell performance is presented. Experimental parametric campaigns were carried out using a button anode supported Solid Oxide Fuel Cell with an active area of about 2 cm^2. A practical zero-dimensional mathematical model based on low and high voltage approximations of the Butler-Volmer equations was used starting from an experimental current–voltage dataset to obtain polarization curve parameters representing different physical phenomena associated with the cell. To validate the obtained results and gain additional information, electrochemical impedance spectroscopy measurements and distribution of relaxation times analysis were performed both in open circuit voltage and underload at 0.5 A/cm^2. Finally, from the fitted parameters, it was possible to derive dimensionless charge transfer coefficients related to the most probable reaction mechanisms occurring in the cell, equal to 2 for the anodic process and 3.5 for the cathodic process. Moreover, from the results the obtained exchange current densities range from 0.024 A/cm^2 to 0.048 A/cm^2 for O_2 reduction and from 0.012 A/cm^2 to 0.073 A/cm^2 for H_2 oxidation and subsequently, the activation energies equal to 100 kJ/mol and 66 kJ/mol for anodic and cathodic electrochemical processes, respectively.

1. Introduction

Over the past few decades, energy consumption, ever more closely linked to the global economy, has been causing irreparable environmental damage [1]. The need to combine environmental protection [2] and limit the use of depleting fossil fuels [3] is an essential aspect of the sustainable development of our planet. Therefore, the development and use of renewable energies such as solar [4,5] or wind [6,7] play a crucial role in tackling global energy issues. Nonetheless, such resources are intermittent and not the same in all locations; therefore, it is necessary to use other efficient technologies to cover the energy demand permanently. Among these, combined heat and power (CHP) systems based on internal combustion engines (ICE) are consolidated and widely used technologies.

Despite being able to cut down primary energy consumption and limit CO_2 emissions, the use of environmentally clean alternative fuels has a crucial drawback that should be considered [8]. Novel technologies, such as fuel cell systems, have been proposed, combining low CO_2 emission outputs with fuel conversion to electricity, gaining significant attention as a promising energy supply from renewed fuels such as hydrogen [9,10]. Fuel cells exhibit certain advantages: i) high efficiencies (up to 75–85 % vs. 30 % of thermoelectric conversion systems) [11,12], ii) Low or zero CO_2 or hazardous emissions [13,14], iii) suitability for different types of applications, both stationary and mobile [15,16]. Fuel cells can be categorized according to operating temperature between low and high-temperature cells. Among the high temperature cells, solid oxide fuel cells (SOFCs) show a high potentiality due to high current/power densities and global efficiency of up to 85 % when waste heat recovery is considered [12]. Moreover, being more resistant

* Corresponding author.
E-mail address: alessandro.dellera@uniroma1.it (A. Dell'Era).

https://doi.org/10.1016/j.enconman.2023.117877
Received 13 June 2023; Received in revised form 4 November 2023; Accepted 10 November 2023
Available online 20 November 2023

Nomenclature

α_1	Charge transfer coefficient for cathode
α_2	Charge transfer coefficient for anode
B	Symmetry factor
Γ	Regularization parameter for the DRT method ($\Omega\bullet cm^2$)
$\underline{\nu}$	Number of times rate determining step repeats
E_0	OCV obtained from experimental conditions (V)
E_a	Activation energy(kJ/mol)
F	Faraday Constant (96,500C/mol)
j	Current density (A/cm^2)
j_0	Exchange current density (A/cm^2)
j_{lim}	Diffusion current density (A/cm^2)
n	Number of electrons involved in the rate determining step
n_1	Number of electrons involved in the reduction process
n_2	Number of electrons involved in the oxidation process
$\overline{n}_1$	Number of electrons involved before the rate determining step for the cathode
$\overline{n}_2$	Number of electrons involved before the rate determining step for the anode
O_{ads}	Oxygen adsorbed
P_0	Fitting parameter that represents the activation polarization resistance ($\Omega\bullet cm^2$)
P_1	Fitting parameter that represents ohmic electrolyte resistance ($\Omega\bullet cm^2$)
P_2	Pre-logarithmic term that takes into account the reaction mechanisms via charge transfer coefficients (V)
P_3	Fitting parameter that takes into account both reaction mechanisms (via charge transfer coefficients) and anodic and cathodic reaction kinetics (via exchange currents densities) (cm^2/A)
P_{1a}	DRT peak related to the ionic conduction of $O2^-$ ions going through the YSZ matrix of the anode functional layer in a range between 800 and 4000 Hz
P_{1c}	DRT peak attributed to the oxygen reduction (O_2/O_2^-) determined by a charge transfer mechanism from around 17 to 78 Hz
P_{2a}	DRT peak indicates charge transfer phenomena due to the fuel oxidation in the internal triple-phase boundary (TPB) region from around 78 to 800 Hz
P_{2c}	DRT peak related to oxygen ions diffusion through the porous structure place between 0.1 and 1 Hz
P_{3a}	DRT peak 1 to 17 Hz occurs in the open porosity of anode substrate
R	Gas constant (J/mol•K)
T	Absolute Temperature (K)
$V_{Cell,\Delta V>50}$	Cell Voltage when potential drops are below 50 mV (mV)
$V_{Cell,\Delta V\leq 50}$	Cell Voltage when potential drops are below 50 mV (mV)
$V_{Cell,\Delta V=50}$	Cell Voltage when potential drops are equal to 50 mV (mV)
Z'	Real part of the impedance ($\Omega\bullet cm^2$)
Z''	Imaginary part of the impedance ($\Omega\bullet cm^2$)4res

Acronyms

0D	Zero-dimensional
CHP	Combined heat and power
CV	Coefficient of variation
DRT	Distribution of relaxation times
ECM	Equivalent circuit model
EIS	Electrochemical impedance spectroscopy
GDC	Gadolinia doped ceria
ICE	Internal combustion engine
LSC	Lanthanum strontium cobaltite
MFC	Mass flow controller
OCV	Open circuit voltage
RDS	Rate determining step
SOFC	Solid oxide fuel cell
TBP	Triple phase boundary
YSZ	Yttrium-stabilized zirconium

to pollutants, they are also suitable for use with biofuels other than hydrogen, such as syngas [17,18]. Definitely, SOFCs represent a valid and clean alternative to ICE in CHP systems [19,20].

In order to understand the operation of SOFC systems under different operating conditions and to extend, simplify and speed up the data analysis, investigators have focused their attention on different modeling approaches that involve physical, statistical, and physical-empirical methods [21]. In this regard, considering that impedance analysis could be a suitable strategy to characterize the electrochemical process within the cell at a specific voltage condition, I-V curves could better represent the performance cell in a broad range of operating voltage. Thus, simulating I-V curves obtained from realistic experimental conditions could achieve a more reliable comprehension of SOFC. For instance, Wang et al. developed a polarization modeling by fitting experimental I-V curves obtained by changing the oxygen partial pressure at the cathodic side in order to separate different polarization contributions found in the cell overpotential, such as ohmic, activation, anodic and cathodic concentration [22]. Similarly, Sahli et al. and Bianchi et al. proposed thermodynamic cell model simulations to determine the polarization losses, displaying the capacity to represent the effect of operating parameters on the potential cell [23,24], while Kuboyama et al. isolated polarization losses through an equivalent circuit model (ECM) and electric charge analysis at the cathode [25].

Furthermore, it is important to stress that some parameters used for modelling are usually taken from the literature to simulate and verify the performance of the cell, such as the activation energy (E_a) [26] or even the exchange current densities (j_0) [27–29] Therefore, those parameters, in some cases, are used to reduce the number of variables and facilitate the equation-solving procedure in order to focus on other aspects of the cell, such as the study of the anodic diffusion polarization [30] or estimation through the fitting of ionic conductivity of the electrolyte, porosity/permeability of the anode support layer, tortuosity and pore diameter [31]. In this concern, Nakajo et al. have assumed a reaction mechanism with the relative rate-determining steps to reduce the number of unknown variables, even if it does not seem to be the one that fits very close to the experimental data [32].In contrast, in our work, the charge transfer coefficient relating to the limiting step is chosen based on the best fitting produced. It is worth noting that this does not mean having univocally determined the reaction mechanism but only having identified the limiting steps among some reaction mechanisms, whose relative anodic and cathodic charge transfer coefficients determine the optimal fitting.

Other investigations focused on understanding SOFC behavior have used available literature and performed specific experimental measurements to determine parameter values subsequently used to feed the model fitting [33]. Those experimental measurements attempt to feature the behavior of the global cell in order to understand local mechanisms occurring on each electrode, which implies specific studies on a single electrode by using half-cells [34]. However, this strategy presents some issues related to the intrinsic complexity of positioning or creating a reference electrode inside the cell [35]. On the other hand, in other cases, actual empirical expressions are even used [36,37]. Moreover, there are several papers that use mathematical models of different complexity from 0D to 3D, but in this work, it is possible to highlight

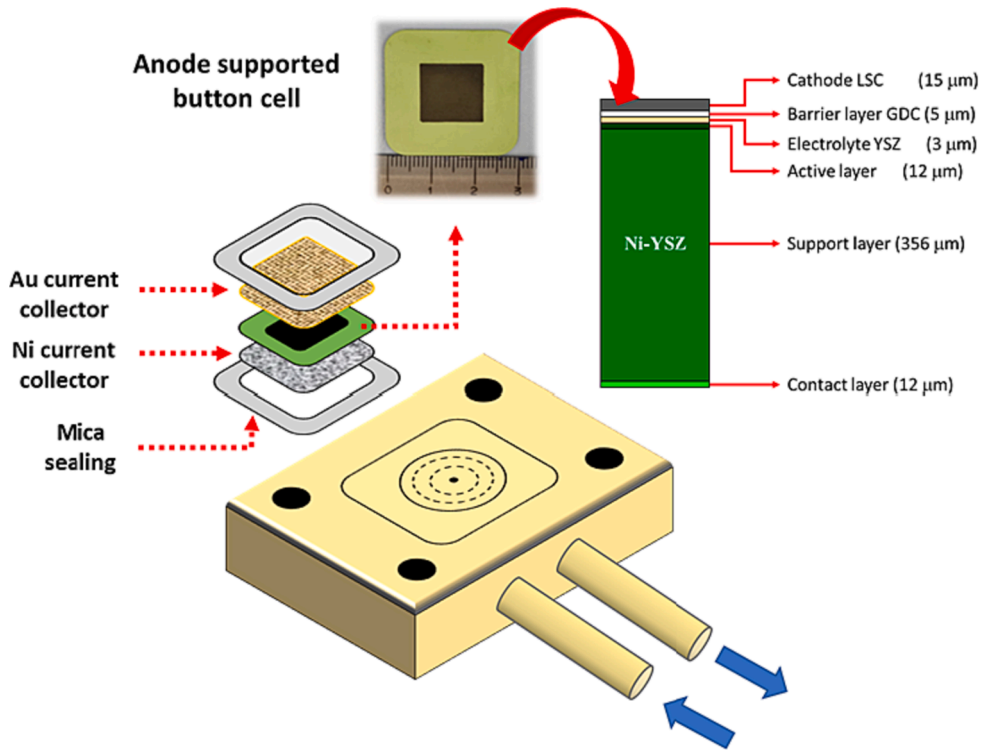

Fig. 1. Details of the button cell and ceramic SOFC test housing used during the test campaign.

that all the electrochemical parameters, characterizing an assembled SOFC cell, have been found by means of the fitting procedure of experimental data obtained in different operating conditions without using the literature as parameters value source, but only as comparison validation.

Indeed, the present investigation is focused on employing effectively and usefully two different approximations of the Butler-Volmer equation to determine all the parameters characterizing an electrochemical device such as a solid oxide fuel cell (SOFC). Considering both approximations over different current and voltage ranges and assuming values for the anodic and cathodic charge transfer coefficients that produced the best fitting, it has been possible to determine the exchange current densities of the two electrodes and the E_a for both the anodic and cathodic processes.

Moreover, electroanalytical analysis has been used to evaluate SOFC performance and its constraints. For example, the single anodic and cathodic effects in electrode resistances combining electrochemical impedance spectroscopy (EIS) with ECM fitting and analysis have been investigated [22]. Although EIS has been considered a notable tool to determine polarization resistances caused by the operating parameters in featured electrochemical systems (batteries, electrolyzers, SOFCs), SOFC systems are strongly influenced by the operating conditions varying their polarization resistances (activation, ohmic and diffusive) in determining times of process, being a critical aspect when it comes to separating a single effect from operating conditions. Since this methodology could cause unsuccessful outcomes due to the overlapping of anodic and cathodic processes [35,38], implementing the reference electrode could also be proposed as an alternative for splitting anodic from the cathodic contribution, even if, as said before, it could present some difficulties [35]. However, significant drawbacks are still mentioned regarding the gas phase contact with an electrode material, electrode placement, and variations on the potential distribution that result in non-reliable current density and overpotential measurements [38].

Considering the previous-mentioned bottleneck and the complexity of resistive mechanisms in fuel cell systems, distribution of relaxation times (DRT) analysis has been developed to identify anodic and cathodic processes attributable to SOFC resistance losses [38–42]. In this regard, Leonide et al. have identified five processes attributable to polarization losses by means of DRT analysis [39,42], while similar analyses have been followed by Caliandro et al., investigating the contribution of the elementary processes to the total losses through the variation of six operating parameters (temperature, current density, oxygen and steam flow rate at both the respective anode and cathode, total flow rates and gas composition) [43]. Those results clarified the physical contribution represented by peaks, mainly those at mid-frequency regions overlapped by the confluence of electrode mechanisms caused by the oxygen and fuel gas reaction. A remarkable achievement in DRT analysis was obtained by Subotić et al., who studied 10-cell stacks by integrating the previous knowledge available for a single cell. In this sense, DRT analysis featured processes at very similar specific frequencies occurring for both single-cell and stacks, but also analysis at early stages facilitated the determination of irreversible processes that could endanger and decrease the lifetime of SOFC [38].

Based on the above-mentioned statements, this investigation proposes a methodology capable of calculating polarization curve parameters by performing a fitting between a voltage balance equation and experimental I–V curves from SOFC analysis under real operating conditions. The analysis of the electrochemical charge-transfer reaction mechanism and EIS measurements agreed with the numerical findings from fitting, while DRT assessments were performed to analyze better the EIS results, separating each polarization resistance contribution associated with a specific frequency. According to the previously results, the anodic and cathodic exchange current density and activation energy were determined for the SOFC system.

2. Materials and methods

In this section, information is provided regarding the equipment used, as well as the various tests performed on the SOFC. Furthermore, the polarization model adopted to perform the fitting analysis is presented in detail.

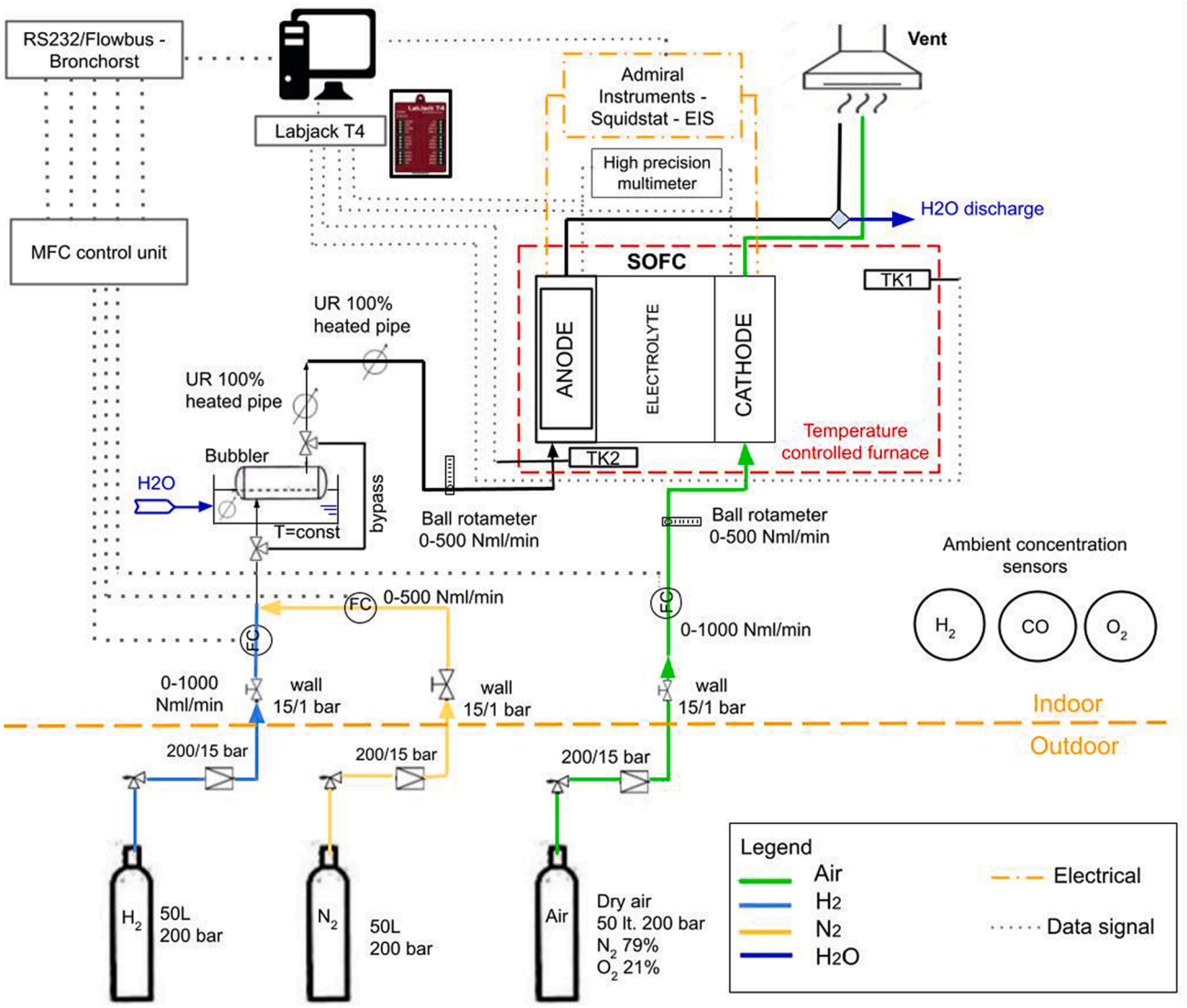

Fig. 2. Experimental setup layout for SOFC test.

2.1. Solid oxide fuel cell features and test rig

An intermediate temperature commercial anode supported square button cell has been used to obtain the experimental dataset at varying temperatures (650, 675, and 700 °C) and hydrogen concentrations at the anode inlet (15, 25, 50, 75, and 90 %). The anode supported button cells consist of a ceramic–metal composite with the following composition Ni-YSZ/YSZ/GDC/LSC. The fuel oxidation occurs at the anode side, which is made of Ni-yttria-stabilized zirconia (Ni-YSZ) divided into contact, support and active layers with a total thickness of around 400 μm. The 15 μm-cathodic layers made of lanthanum strontium cobaltite (LSC) is in charge of oxygen reduction when airflow is in contact. Both anodic and cathodic layers are separated by yttria-stabilized zirconia (YSZ) as electrolyte (3 μm) and gadolinia doped ceria (GDC) acting as a diffusion barrier. The anodic and cathodic active surface of the cell has dimensions of 14 × 14 mm. Fig. 1 shows the details of the fuel cell and its schematic internal structure.

A complete ceramic housing made of alumina purchased from CHINO Corporation has been used. The holder can accommodate either button cells or 5 × 5 cm-square cells by changing only the gas distribution plate. Moreover, it optimizes thermal and electrical insulation, avoiding steel poisoning during operations, compared to metal holders that are conventionally used. The closing of SOFC assembly is another crucial step to guarantee proper gas tightness: it is achieved by aligning a mica sealing between each gas distribution plate and button cell, followed by a mechanical closing composed of ceramic screws, nuts and springs; all this system is tightened to 12 cNm. This procedure focused on maintaining a proper gas distribution and reducing potential gas leakage problems. Nickel and gold mesh current collectors are used for the anode and cathode sides, respectively (Fig. 1). The electrical current is brought outside through platinum wires, which are connected to the current collectors. A thermocouple is pre-installed inside the holder in order to acquire the cell temperature.

Fig. 2 illustrates the test rig employed in the experimental campaign, which incorporates a furnace, gas feeding pipeline, data acquisition and control system, electrochemical analysis system, and a solid oxide fuel cell (SOFC) unit. A CarboliteGero CWF 11/13 3216 furnace was used during the experimental campaigns. The temperature control, which consists of cooling and heating ramps at 1 °C/min, was guaranteed through a proportional–integral–derivative (PID) controller, checking the temperature from thermocouples TK1 and TK2 (type K) installed inside the chamber and the anode inlet, respectively.

The gas feeding system consists of three different lines connected to steel storing cylindrical gas tanks (50L × 200 bar) containing pure technical gas (N_2, H_2) and air (79 % N_2 and 21 % O_2). The operational pressure of the mass flow controllers (MFCs) (Bronkhorst El-Flow),

Table 1
Experimental array assessing different H_2 concentrations at the anode side (15, 25, 50, 75 and 90 %vol) and temperatures (650, 675 and 700 °C) using an active surface area of about 2 cm^2.

Temperature		650, 675 and 700 °C				
H_2 variations (%vol)		**15**	**25**	**50**	**75**	**90**
Anode flow	H_2	11.25	18.75	37.5	56.25	67.5
($Nml \bullet min^{-1} \bullet cm^{-2}$)	N_2	63.75	56.25	37.5	18.75	7.5
	Total	75				
Cathode flow	Total	**Air**				
($Nml \bullet min^{-1} \bullet cm^{-2}$)		125				

located at the inlet, is approximately 2 bar as the technical gases are transferred from 200 bar tanks. A gas mixture consisting of H_2 and N_2 was fed to the anode while the air was supplied as the oxidant to the cathode side by regulating both the gas pressure and mass flow rate at the inlet.

The input signals from the instrumentation were monitored through the Admiral proprietary software and in-house-made LabVIEW program, which collects and visualizes all the data from controllers and sensors (thermocouples, MFCs and voltmeters). Furthermore, the performance of the SOFC unit was analyzed by a potentiostat/galvanostat Admiral Instruments Squidstat Cycler 1404 with four independent channels along with two pairs of electrodes and sensing auxiliary wires in order to perform polarization curves and EIS measurements. This versatile equipment, in galvanostatic mode, can supply current ranging from 0 to 5 A and maximum accuracy and resolution of about 115 μA and 2.70 μA, respectively. In the case of the potentiostatic mode, it can measure up to 5 V with an accuracy near 2 mV and a resolution close to 11 μV. In particular, in the performed EIS measurements, potentiostatic mode was used for OCV conditions with an amplitude of ±10 mV as an excitation signal, while galvanostatic mode was employed in underload conditions at 1 A with an amplitude of ±100 mA as excitation signal. In both cases, the frequency ranged from 10 kHz to 100 mHz with 50 steps. In addition, a high precision voltmeter (Mastech MS8229) was permanently used to measure voltage outputs without interfering with the electrical system. Finally, it is worth adding that the fitting process does not require much computational resources and experimental data used in the fitting do not require any pre-processing procedure. Regarding resource requirements, the used model is a 0D model, and it can be simply compiled and solved by some mathematical software such as MatLab, MathCad or Origin. In this work, MatLab was used.

2.2. Experimental campaign

Several tests were conducted to obtain experimental data required for the model fitting. Start-up, shut-down and anode reduction phases have been conducted following the procedures reported in our previous work [44]. Different operating conditions (hydrogen concentration and temperature) were evaluated, as seen in Table 1. The total flow rate at the anode was kept constant at 150 Nml/min by fixing the H_2 and N_2 flow ratio. At the cathode side, an airflow rate of 250 Nml/min with a nominal composition of 21 % O_2 and 79 % N_2 was used. From Table 1 and Fig. 3, considering the inlet anode flow and delivered current it is possible to state that the cell always works in over stoichiometric oxygen conditions.

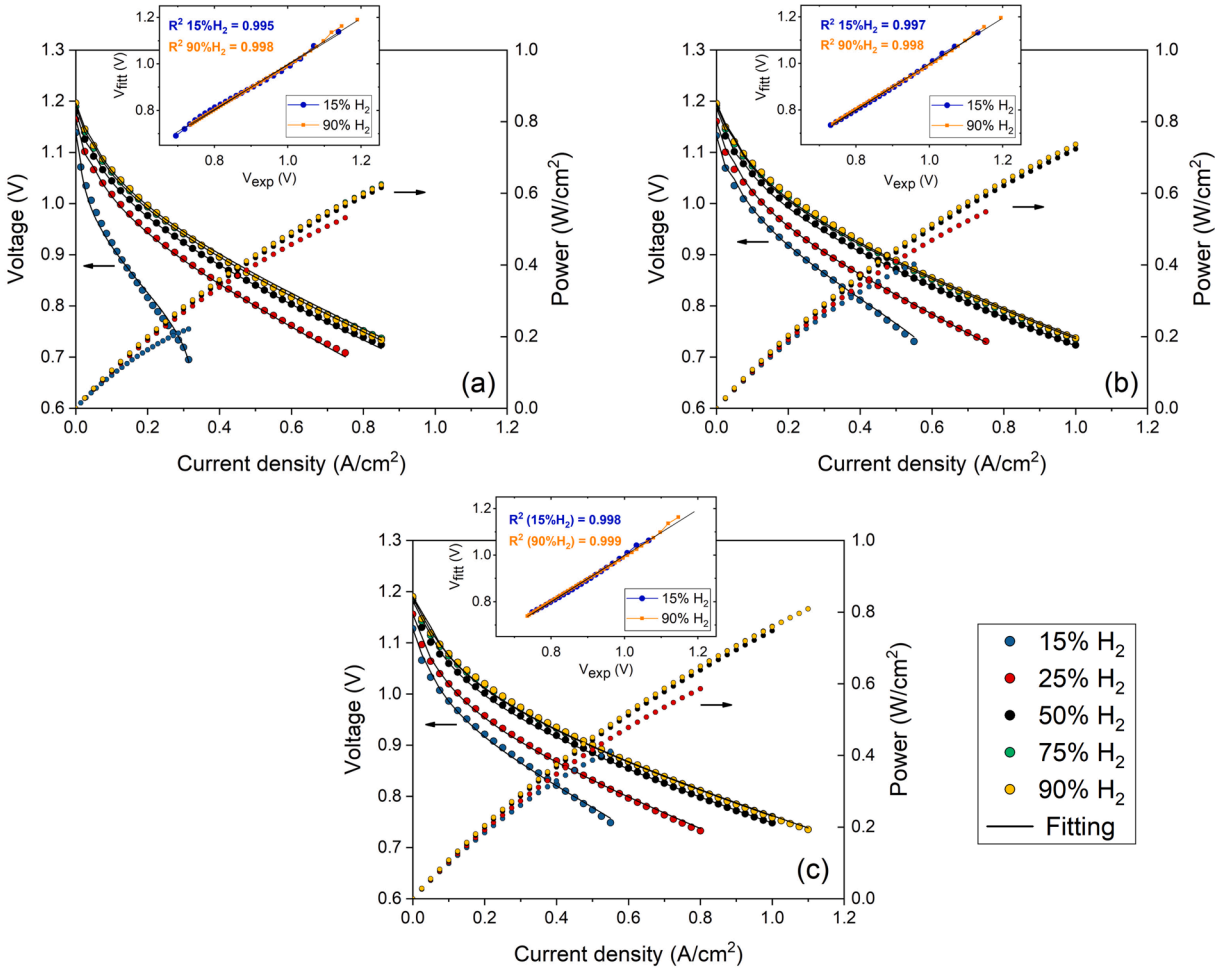

Fig. 3. Polarization, fitting and power curves for different hydrogen concentrations at (a) 650 °C, (b) 675 °C and (c) 700 °C.

Table 2
Polarization curves parameters values for P_0, P_1, P_2, and P_3.

H_2 (%)	15				25				50				75				90			
T (°C)	P_0	P_1	P_2	P_3	P_0	P_1	P_2	P_3	P_0	P_1	P_2	P_3	P_0	P_1	P_2	P_3	P_0	P_1	P_2	P_3
650	4	0.26	0.061	73	2.4	0.26	0.061	53	2	0.26	0.061	34	1.7	0.26	0.061	26	1.65	0.26	0.061	23
675	2.2	0.21	0.063	55	1.9	0.21	0.063	40	1.5	0.21	0.063	28	1.4	0.21	0.063	22	1.35	0.21	0.063	19
700	1.8	0.18	0.065	43	1.55	0.18	0.065	31	1.2	0.18	0.065	20	1.1	0.18	0.065	15	1	0.18	0.065	14

Polarization curves were generated by increasing the current in steps of 100 mA, beginning from the open circuit voltage (OCV) to a limit potential of 700 mV. This potential limit has been selected according to the range of nominal working conditions of the cell suggested by other investigations [39]. In addition, impedance measurements were performed by operating the EIS module in both potentiostatic mode for OCV and galvanostatic mode for underload conditions at 1 A. The EIS results were subsequently analyzed by the DRT using a free MatLab toolbox [45] with the Gaussian discretization method and a regularization parameter (λ) equal to 1×10^{-3} [46]. That analysis was used to identify each polarization resistance with respect to a characteristic frequency.

2.3. Model description

The developed model takes into account activation, ohmic and concentration overpotentials. In order to achieve the best fitting for each current density value, Eq. (1) is used for the initial 50 mV decrease in potential values, while Eq. (2) is used when the potential drop exceeds 50 mV.

$$V_{Cell,\Delta V\leq 50} = E_0 - (P_0 + P_1) \bullet j \tag{1}$$

$$V_{Cell,\Delta V>50} = V_{Cell,\Delta V=50} - P_1 \bullet j - P_2 \bullet ln(P_3 j) - \frac{RT}{nF} \bullet ln(1 - \frac{j}{j_{lim}}) \tag{2}$$

R is the gas constant, T is the cell operating temperature, F is Faraday's constant, and n is the number of electrons involved in the redox reaction. In the case of $V_{Cell,\ \Delta V\leq 50}$ and $V_{Cell,\ \Delta V>50}$, they represent the cell voltage when potential drops are below and above 50 mV, respectively, whereas $V_{Cell,\ \Delta V=50}$ is the cell voltage calculated from Eq. (1) when the potential drop is equal to 50 mV. E_0 is the OCV obtained from experimental conditions, j is the current density, and P_0, P_1, P_2 and P_3 correspond to polarization curve parameters.

In Eq.1, activation losses are considered by linearization of the Butler-Volmer equation (Eq. (3), while in Eq. (2), a Tafel expression that accounts for both anodic and cathodic activation overvoltage is used (Eq. (4) [47]. Ohmic losses are expressed with the ohmic law considering the electrolyte resistance (Eq. (5). For low H_2 concentrations (15 % and 25 %), it was also necessary to consider the diffusion overvoltage term that considers the diffusion limit current density (j_{lim}, Eq.6). The j_{lim} value shows a direct relationship with the temperature, that is, when it increases the j_{lim} value increases. The j_{lim} value was helpful for lower hydrogen concentrations than 25 %; once the hydrogen concentration increases, such a value makes the diffusive term negligible.

$$\eta_{act\Delta V\leq 50} = (P_0) \bullet j \tag{3}$$

$$\eta_{act\Delta V>50} = P_2 \bullet ln(P_3 j) \tag{4}$$

$$\eta_{ohm} = P_1 \bullet j \tag{5}$$

Table 3
Limit current density values for low hydrogen concentration.

T (°C)	650	675	700
H_2 (%)	J_{lim} (A/cm^2)		
15	0.33	0.75	0.85
25	1.55	1.65	1.80

$$\eta_{diff} = \frac{RT}{nF} \bullet ln(1 - \frac{j}{j_{lim}}) \tag{6}$$

P_0 represents the activation polarization resistance parameter (Eq. (7).

$$P_0 = \frac{RT}{F}\left(\frac{1}{n_1 j_{01}} + \frac{1}{n_2 j_{02}}\right)(\Omega\bullet) \tag{7}$$

Where j_{o1} and j_{o2} are the exchange current densities for the cathodic and anodic components, and n_1 and n_2 are the number of electrons involved in the reduction and oxidation process at the cathode and anode, respectively.

The ohmic electrolyte resistance is represented by the parameter P_1.

P_2 is a pre-logarithmic term that takes into account the reaction mechanisms via charge transfer coefficients (Eq. (8)).

$$P_2 = \frac{RT}{F}\left(\frac{1}{\alpha_1} + \frac{1}{\alpha_2}\right)(\text{V}) \tag{8}$$

Where α_1 and α_2 are the charge transfer coefficients for cathodic and anodic processes, respectively.

Finally, P_3 takes into account both reaction mechanisms (via charge transfer coefficients) and anodic and cathodic reaction kinetics (via exchange currents densities), as shown in Eq. (9).

$$P_3 = \left(\frac{1}{j_{01}}\right)^{\frac{\alpha_2}{(\alpha_1+\alpha_2)}}\left(\frac{1}{j_{02}}\right)^{\frac{\alpha_1}{(\alpha_1+\alpha_2)}}(cm^2/\text{A}) \tag{9}$$

E_0 and j are experimental inputs, while $V_{Cell,\ \Delta V\leq 50}$, $V_{Cell,\ \Delta V>50}$, $V_{Cell,\ \Delta V=50}$ and polarization curves parameters are the outputs obtained by the fitting that enables the most accurate approximation of the experimental data.

3. Results and discussion

In this section, after a brief analysis of the experimental data, the output of fitting is presented, such as the values found for the polarization curve parameters and their trends. The obtained results are then validated through additional impedance tests using the distribution of relaxation time (DRT) to identify the characteristic frequencies associated with anodic and cathodic processes at different operating conditions. Subsequently, the results obtained for the fitting parameters were linked with the most probable anodic and cathodic reaction mechanisms.

3.1. Cell performance and polarization curve parameters

Fig. 3 presents the results of the experimental tests and the model fitting, showing the cell polarization and electrical power curves.

The polarization curves reveal a correlation between hydrogen percentage and the disparity in voltage and power performance. Notably, when a cell works with a 50 % hydrogen supply, it demonstrates an acceptable performance. Also, it is observed that further H_2 concentration increase, beyond that value, does not yield significant performance enhancements. Additionally, the trend of power curves shows that the maximum power achievable by the system corresponds to lower operating voltage values, outside the range of nominal working conditions generally used in this kind of application (0.7 V). A fitting curve was

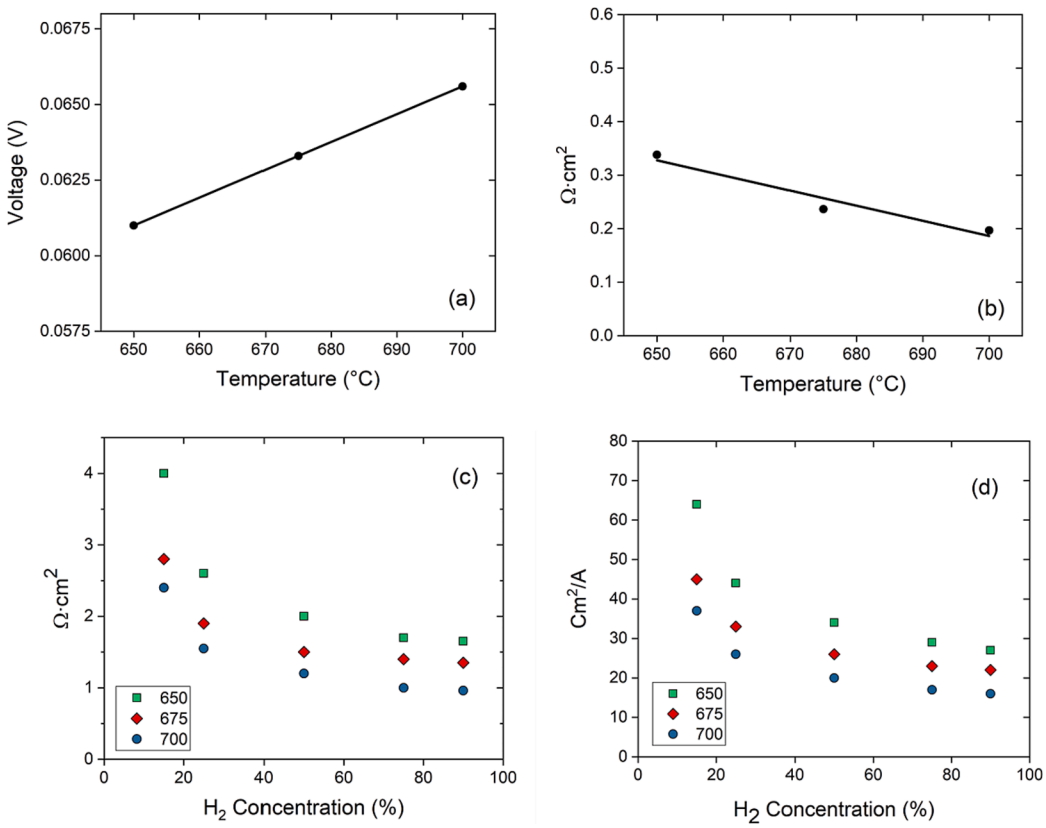

Fig. 4. Polarization curves parameters (a) P_2, (b) P_1, (c) P_0, and (d) P_3 when temperature or hydrogen concentration change.

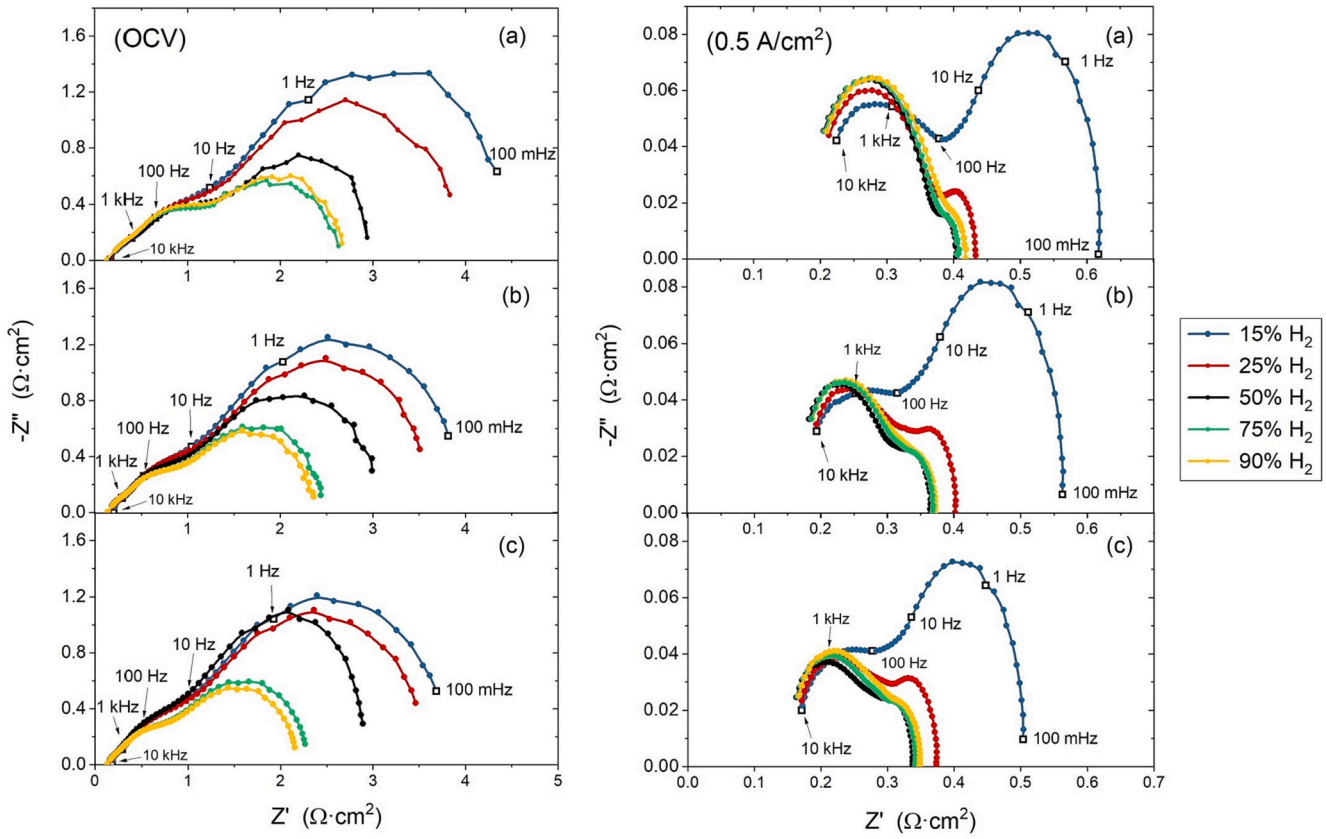

Fig. 5. Nyquist plot performed in OCV and at 0.5 A/cm^2 using different dry hydrogen concentrations from 15 % to 90 % at (a) 650 °C, (b) 675 °C, and (c) 700 °C.

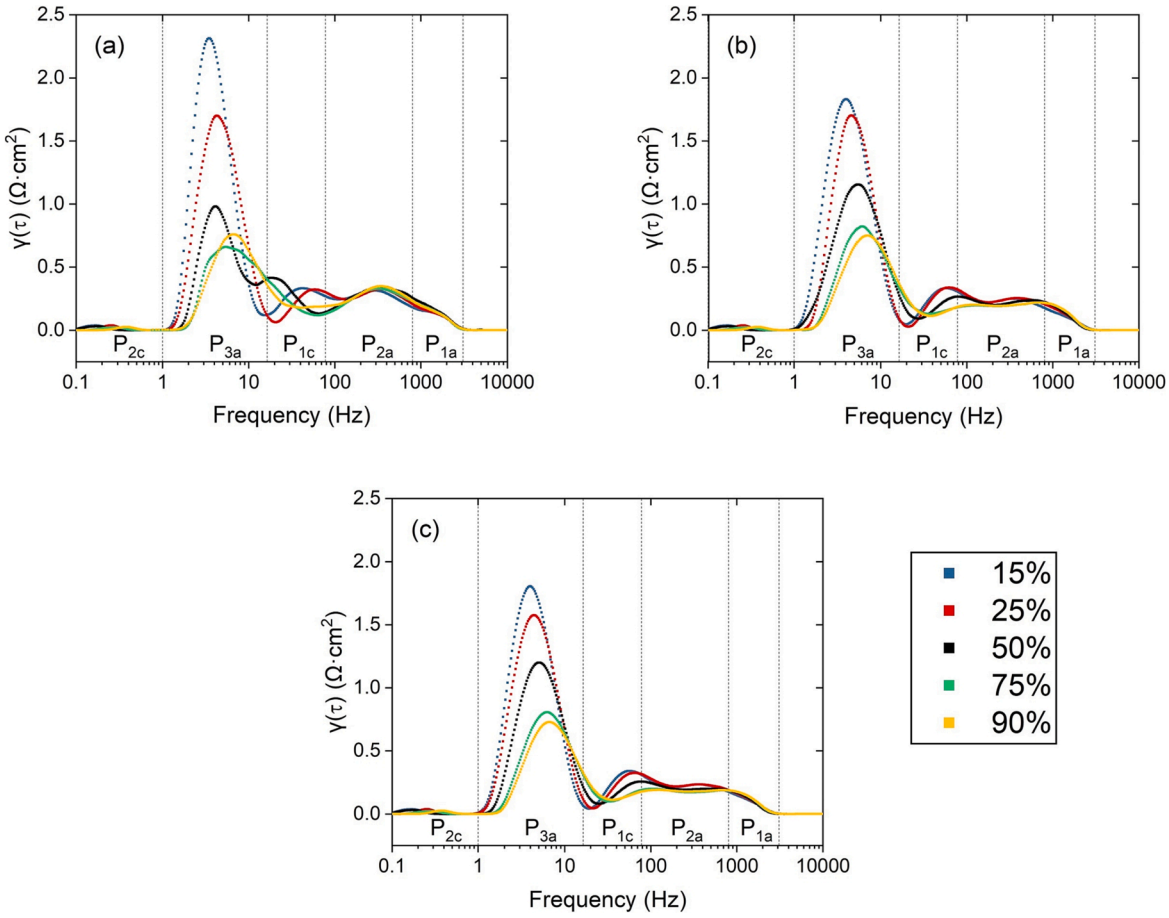

Fig. 6. DRT curves at different dry hydrogen concentrations from 15 % to 90 % in OCV conditions at (a) 650 °C, (b) 675 °C, and (c) 700 °C.

generated for each polarization curve, and numerical values for P_0, P_1, P_2 and P_3 were derived and summarized in Table 2. Moreover, the j_{lim} values reported in Table 3 change coherently since the temperature and hydrogen percentage normally favor the diffusive phenomena. As mentioned above, for hydrogen percentages higher than 25 %, it was not possible to determine the j_{lim} values from fitting due to negligible diffusion phenomena in the used current range. In addition, a parity plot for polarization curves obtained at 15 % and 90 % H_2 has been embedded into graphs shown in Fig. 3 to quantify, by the correlation coefficient (R^2), the quality and the efficiency of the fitting, as well as performed in [33]. The R^2 parameters obtained for the polarization curves within 15 % and 90 % H_2 are equal or in between the values reported on the graph.

Fig. 4 shows the polarization curves parameters P_2, P_1, P_0, and P_3 as temperature or hydrogen concentration changes. The P_0 value decreases as the temperature or the H_2 concentration increases. From its formulation, P_0 exhibits an inverse relationship with the exchange current densities, which are related by electrode kinetics and consequently directly proportional to the concentration of the hydrogen and oxygen species, respectively. Similarly, the exchange current density value increases as the temperature rises due to the corresponding increase in electrochemical kinetics. P_1, being an intrinsic parameter of the material of the cell, is not affected by the H_2 concentration, but decreases with increasing temperature due to the enhanced ion mobility. As expected from Eq. (8), P2 depends solely on temperature and increases with it. Finally, P_3 shows a decrease with increasing temperature or hydrogen content. This behavior can be attributed to the same explanation as parameter P_0, as both P_3 and P_0 are connected to the exchange current densities.

3.2. Electrochemical impedance spectroscopy and distribution relaxation times analysis

Electrochemical impedance spectroscopy analyses have been performed to enhance the understanding of cell behavior and validate parameters P_0 and P_1. The obtained data were subsequently processed using the distribution of relaxation times method. These tests were conducted under two conditions: i) open circuit and ii) under load with a current density of 0.5 A/cm^2.

3.2.1. Electrochemical impedance spectroscopy analysis

Fig. 5 displays the EIS curves considering the variation of hydrogen concentration at different temperatures for OCV and 0.5 A/cm^2 conditions. From the Nyquist plot it is possible to identify the ohmic resistance as the first intercept between the EIS curve and the real axis. The polarization resistance, which takes into account both activation and diffusion losses, can instead be identified by the difference between the second and first intersection of the EIS graph with the real axis.

Regarding polarization resistance, its values decrease from OCV to under load because when current flows, the potential value assumed by the electrode determines the activation of the electrode itself [48]. At a current density of 0.5 A/cm^2, the performance remains stable when the percentage of H_2 is equal to or >50 %. However, by decreasing the hydrogen concentration, a slight variation is observed at 25 %, which is more evident at 15 %. This behavior suggests that diffusive phenomena are much more evident at lower H_2 concentrations. The mean value in OCV conditions is around 3 Ω·cm^2; meanwhile, in underload conditions, the mean value is 0.26 Ω·cm^2. This range is in accordance with the mean value calculated from Table 2 for the activation resistance parameter (P_0) equal to 1.783 Ω·cm^2. Moreover, ohmic resistances show no evident

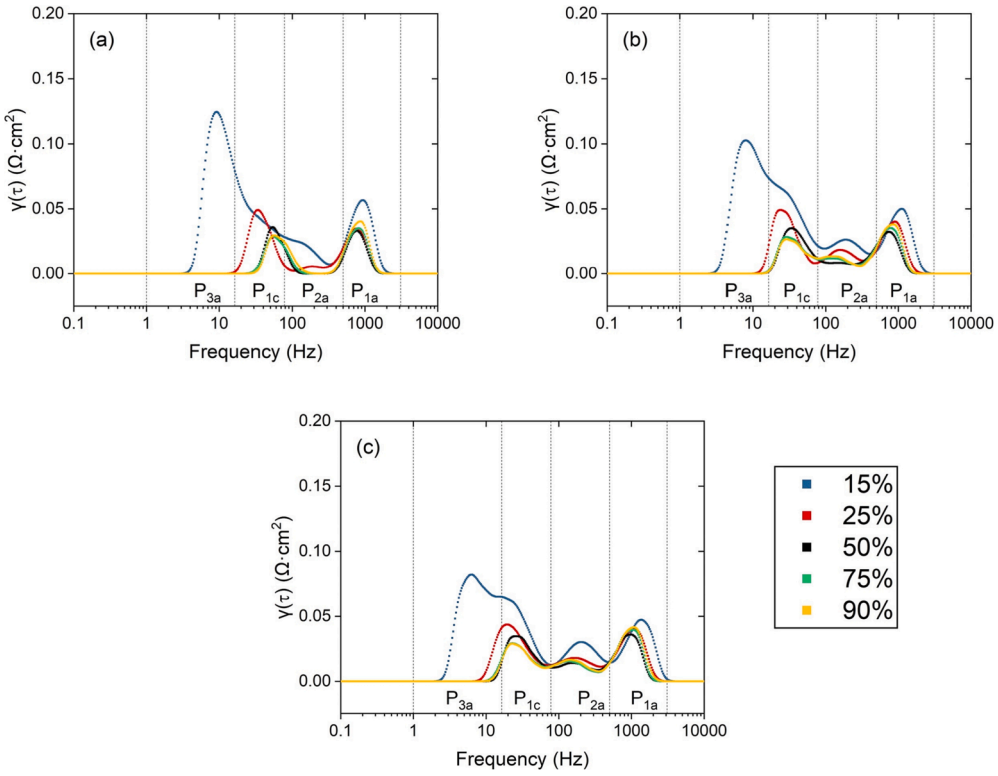

Fig. 7. DRT curves at different dry hydrogen concentrations from 15 % to 90 % using 0.5 A/cm^2 current density condition at (a) 650 °C, (b) 675 °C, and (c) 700 °C.

changes from OCV to 0.5 A/cm^2, to be around 0.2 Ω·cm^2. This result is aligned with the mean value calculated from Table 2 for the ohmic resistance parameter (P_1) equal to 0.216 Ω·cm^2. Accordingly, the order of magnitude of P_0 and P_1 found with the fitting procedure is consistent with the average values found with EIS.

3.2.2. *Distribution relaxation times analysis*

DRT analyses, considering OCV and 0.5 A/cm^2, have been performed in order to represent qualitatively the experimental conditions used for modeling the system. Characteristic times are associated with anodic and cathodic processes (charge transfer, mass transport, diffusion, gas conversion, etc.) within the internal thin Ni-YSZ/YSZ/GDC/LSC microstructure of cell. In agreement with the literature [38,39], six characteristic peaks on the DRT diagram have been attributed to those anodic and cathodic mechanisms in a range of frequencies. Three peaks associated with the anodic process involve peak 1 (P_{1a}) related to the ionic conduction of O^{2-} ions going through the YSZ matrix of the anode functional layer in a range between 800 and 4000 Hz, peak 2 (P_{2a}) indicates a charge transfer due to the fuel oxidation in the internal triple-phase boundary (TPB) region from around 78 to 800 Hz and peak 4 (P_{3a}), representing the mass transport phenomenon related to the gas diffusion process, from 1 to 17 Hz occurs in the open porosity of anode substrate. Moreover, analogous processes are represented by peak 3 (P_{1c}) and peak 5 (P_{2c}) at the cathodic electrode. The former is attributed to the oxygen reduction (O_2/O^{2-}) determined by a charge transfer mechanism from around 17 to 78 Hz, while the latter is the contribution of the oxygen ions diffusion through the porous structure place between 0.1 and 1 Hz. Finally, a sixth anodic peak, suggested from literature but not seen in these results, indicates the gas conversion at very low frequencies [39].

Based on the above-mentioned, the effect of operative parameters on SOFC performance can be studied from the point of view of polarization resistances. In this context, three different cases, (*i*) fuel composition, (*ii*) operating current density, and (*iii*) temperature, were considered to analyze the variation of DRT curves. From Fig. 6, it is possible to observe that the hydrogen dilution in N_2 shows a significant increase in the resistive processes, mainly related to the anodic mass transport phenomenon (P_{3a}) between 1 and 17 Hz. This behavior, not seen on other DRT peaks, can be attributed to nitrogen inhibition, triggering the increase of activation overpotentials for low current densities or OCV conditions [38]. By increasing the hydrogen concentration, P_{3a} changes in both intensity and frequency with a slight shift toward high frequencies; instead, the others showed negligible variations as temperature and hydrogen concentrations changed.

Fig. 7 shows polarization resistances on DRT curves using a 0.5 A/cm^2 current density. As a first observation, a general decrease in DRT resistances is notable, which is associated with the shrinking of the peak's amplitude compared with those obtained in OCV. When 0.5 A/cm^2 is applied, P_{2a} and P_{1c} decrease in intensity, while P_{3a} and P_{2c} virtually disappear as a result of both steams generated from the current passing through the cell and the oxygen diffusion, respectively. When SOFC is increasingly fueled with hydrogen content, the steam influence on the impedance decay is much more evident at hydrogen content higher than 15 % since the steam formation should limit the nitrogen effect, promoting hydrogen diffusion. Accordingly, the favorable conditions promoted by steam formation under current load conditions suggest the disappearance of those peaks at frequencies lower than 1 Hz and about 10 Hz, except for very low hydrogen content (15 %) [38,48].

Finally, from DRT curves (Fig. 7a–c), by applying a current density, anodic and cathodic polarization losses decrease and peaks also shift towards higher frequencies, suggesting the diminishing of the time constant. In these conditions, decreasing the time constant regarding electrochemical processes likely entails a kinetic improvement, while much slower kinetic processes could be correlated to longer time constants such as oxygen ions diffusion or gas conversion [38,48].

3.3. *Mechanism and activation energy*

The fitting analysis contributed to understanding the performance of the fuel cell under different operating conditions. These parameters

should be better analyzed and compared with the literature. An attempt to understand and validate those values could be focused on calculating j_{01} and j_{02}, which are intrinsically linked with the cathodic and anodic reaction mechanisms. The reaction mechanisms in electrochemistry (as well as for SOFCs) are usually described by dimensionless charge transfer coefficients, such as α_1 and α_2 values, which explains the fraction of overpotential that an electrochemical process requires to surpass the energy barrier at the cathode/anode-electrolyte interface defining the direction of reaction (reactants to products or vice versa) and that depend on process rate-determining step (RDS) determination [49,50]. The assumption of values for the two charge transfer coefficients implies hypothesizing potential kinetic mechanisms and their respective rate-determining steps, which appear in the P2 term (equation (8)) of the polarization curve equation (2). Thus, fitting the polarization curve and determining the P2 term allows the validation of the initial hypothesis. However, although this assumption does not mean the unique determining step for the reaction mechanisms, it is fair to claim that this methodology suggests it can be compatible with the experimental data obtained. Therefore, a screening of possible mechanisms compatible with the experimental data and their fitting was performed.

Several cathodic and anodic mechanisms found in the literature have been considered as follows:

3.3.1. *Mechanisms for oxygen reduction process at the cathode*

Mechanism C1

$$O_2 \rightarrow 2O_{ads} \quad \text{(C1-1)}$$

$$O_{ads} + e^- \rightarrow O^-_{ads} \quad \text{(C1-2)}$$

$$O^-_{ads} \rightarrow O^-_{TPB} \quad \text{(C1-3)}$$

$$O^-_{TPB} + e^- + V_{\ddot{O}} \rightarrow O^x_o \quad \text{(C1-4)}$$

Mechanism C2

$$O_2 + e^- \rightarrow O^-_{2ads} \quad \text{(C2-1)}$$

$$O^-_{2ads} + e^- \rightarrow 2O^-_{ads} \quad \text{(C2-2)}$$

$$O^-_{ads} \rightarrow O^-_{TPB} \quad \text{(C2-3)}$$

$$O^-_{TPB} + e^- + V_{\ddot{O}} \rightarrow O^x_o \quad \text{(C2-4)}$$

Mechanism C3

$$O_2 + e^- \rightarrow O^-_{2ads} \quad \text{(C3-1)}$$

$$O^-_{2ads} \rightarrow O^-_{TPB} \quad \text{(C3-2)}$$

$$O^-_{TPB} + e^- + V_{\ddot{O}} \rightarrow O^x_o + O_{ads} \quad \text{(C3-3)}$$

$$O_{ads} + e^- \rightarrow O^-_{ads} \quad \text{(C3-4)}$$

$$O^-_{ads} + e^- + V_{\ddot{O}} \rightarrow O^x_o \quad \text{(C3-5)}$$

Where $V_{\ddot{O}}$ is the oxygen vacancy in the electrolyte with two positive virtual charges, O^x_o corresponds with the oxygen occupying its natural position in the neutrally charged electrolyte, and TPB is the triple phase boundary of gas, electrode and electrolyte.

Reaction pathways at the anode

Mechanism A1 (hydrogen spillover)

$$O^x_o \rightarrow O^{-2}(YSZ) + V_{\ddot{O}}(YSZ) \quad \text{(A1-1)}$$

$$H_2 \rightarrow 2H_{ads}(Ni) \quad \text{(A1-2)}$$

$$O^{-2}(YSZ) + H_{ads}(Ni) \rightarrow OH^-_{ads}\,(YSZ) + e^- \quad \text{(A1-3)}$$

$$OH^-_{ads}\,(YSZ) + H_{ads}(Ni) \rightarrow H_2O_{ads}(YSZ) + e^- \quad \text{(A1-4)}$$

$$H_2O_{ads}\,(YSZ) \rightarrow H_2O \quad \text{(A1-5)}$$

Mechanism A2 (Oxygen spillover)

$$O^{-2}_{ads}\,(YSZ) \rightarrow O^{-2}_{ads}(Ni) \quad \text{(A2-1)}$$

$$O^{-2}_{ads}\,(YSZ) \rightarrow O_{ads}(YSZ) + 2e^- \text{ before} \quad \text{(A2-2a)}$$

$$O^{-2}_{ads}\,(YSZ) \rightarrow O_{ads}(Ni) + 2e^- \text{ during} \quad \text{(A2-2b)}$$

$$O^{-2}_{ads}\,(Ni) \rightarrow O_{ads}(Ni) + 2e^- \text{ after} \quad \text{(A2-2c)}$$

$$H_2 \rightarrow 2H_{ads}(Ni) \quad \text{(A2-3)}$$

$$H_{ads}(Ni) + O_{ads}(Ni) \rightarrow OH_{ads}(Ni) \quad \text{(A2-4)}$$

$$OH_{ads}(Ni) + H_{ads}(Ni) \rightarrow H_2O_{ads}(Ni) \quad \text{(A2-5)}$$

$$H_2O_{ads}(Ni) \rightarrow H_2O \quad \text{(A2-6)}$$

Mechanism A3 (Interstitial hydrogen)

$$H_2 \rightarrow 2H_i(Ni) \quad \text{(A3-1)}$$

$$H_i(Ni) \rightarrow H^+_i(YSZ) + e^- \quad \text{(A3-2)}$$

$$2H^+_i\,(YSZ) + O^{-2}\,(YSZ) \rightarrow H_2O_{ads}(YSZ) \quad \text{(A3-3)}$$

$$H_2O_{ads}(YSZ) \rightarrow H_2O \quad \text{(A3-4)}$$

These charge transfer coefficient values (α_1 and α_2) were also calculated from the possible cathodic and anodic processes, following the expressions found in [49,50] and assuming possible RDS.

$$\alpha_1 = \alpha_c = \frac{\overline{n_1}}{\underline{\nu}} + n\beta \quad \text{(10)}$$

$$\alpha_2 = \alpha_a = \frac{\overline{n_2}}{\underline{\nu}} + n\beta \quad \text{(11)}$$

Where $\underline{\nu}$, $\overline{n}_{1,2}$, n and β are the number of times RDS repeats or should be repeated, electrons involved before the RDS, electrons involved in the RDS, and symmetry factor, respectively. If it is hypothesized that the RDS is the C3-5 reaction, α_1 should be 3.5, and if RDS is any chemical reaction that takes place after the oxidation reactions in the anodic hydrogen spillover mechanism (e.g., reaction A1-5) or in the anodic mechanism of oxygen spillover (e.g., reaction A2-6), α_2 will be equal to 2. Since the P_2 parameter was defined as 0.063 at 675 °C (Table 2), the constant term (P_2F/RT) easily calculable from Eq. (8), is equal to about 0.79. The latter value is coherent with those cathodic [51,52] and anodic [53,54] mechanisms, which have a RDS for each reaction with α_1 and α_2 values equal to 3.5 and 2, respectively. Those mechanisms describe both the oxygen reduction process at the cathode and the oxidation reactions at the anodic side, describing the mechanisms in three different charge-transfer pathways for each electrode. In the case of the cathode, the oxidation reaction process considers the spillover of oxygen electroactive species (O^- and O^{-2}), which could be adsorbed along the LSC surface to the TPB zone (C1-C3) [51,55]. Furthermore, the hydrogen and oxygen spillover and the hydrogen interstitial have also been associated with the mechanism reaction occurring on the anodic side [54].

Considering Eq. (7) and the cathodic mechanism C3, the total number of electrons involved (n_1) is equal to 4, while oxygen or hydrogen spillover regarding anodic mechanisms, the total number of electrons involved (n_2) is equal to 2. In this context, the term P_0 will be equal to Eq. (12), as follows:

$$P_0 = \frac{RT}{F}\left(\frac{1}{4j_{01}} + \frac{1}{2j_{02}}\right) \quad \text{(12)}$$

The parameter P_3, with the previous α values considered, can be represented in Eq. (13).

$$P_3 = \left(\frac{1}{j_{01}}\right)^{\frac{2}{(5.5)}}\left(\frac{1}{j_{02}}\right)^{\frac{3.5}{(5.5)}} \quad \text{(13)}$$

Based on the previous expressions (Eq. (12) and Eq. (13)), the j_0

Table 4
Cathodic and anodic exchange current density (A/cm^2) calculated using P_0 and P_3 at different temperatures and H_2 concentrations.

H_2 (%)	15		25		50		75		90	
T (°C)	j_{01}	j_{02}	j_{01}	j_{02}	j_{01}	j_{02}	j_{01}	j_{02}	j_{01}	j_{02}
650	0.024	0.012	0.024	0.022	0.024	0.033	0.024	0.042	0.024	0.047
675	0.031	0.018	0.031	0.030	0.031	0.044	0.031	0.053	0.031	0.057
700	0.048	0.019	0.048	0.034	0.048	0.051	0.048	0.066	0.048	0.073

Table 5
Cathodic and anodic activation polarization resistances in Ω•cm^2.

H_2 (%)	15		25		50		75		90	
T (°C)	P_{01}	P_{02}	P_{01}	P_{02}	P_{01}	P_{02}	P_{01}	P_{02}	P_{01}	P_{02}
650	0.828	3.251	0.828	1.805	0.828	1.203	0.828	0.937	0.828	0.838
675	0.659	2.222	0.659	1.365	0.659	0.939	0.659	0.774	0.659	0.722
700	0.437	2.153	0.437	1.237	0.437	0.819	0.437	0.634	0.437	0.577

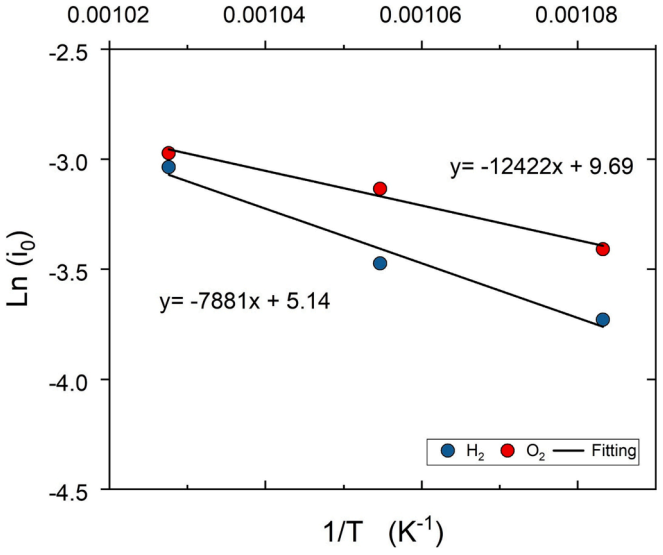

Fig. 8. Activation energy of the cathodic process for 21 % O_2 and the anodic process for 50 % H_2.

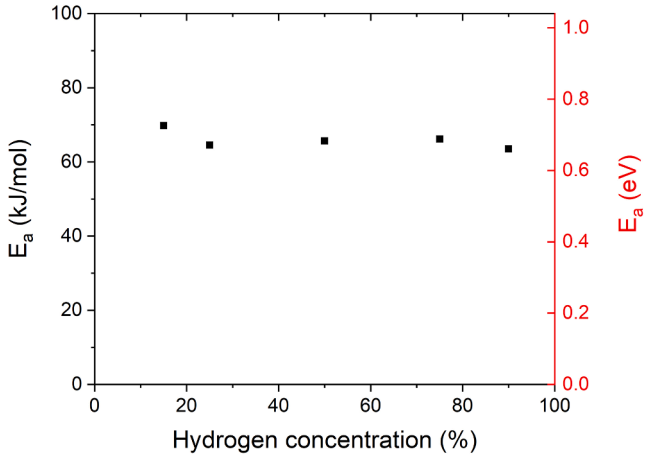

Fig. 9. Values of the activation energy for different H_2 concentrations.

values for the cathodic and anodic process and the related activation polarization resistances at different temperatures and different percentages of H_2 were calculated and listed in Table 4 and Table 5. The obtained results show that the temperature increase causes the increase of the cathodic (j_{01}) and anodic (j_{02}) exchange current density, being more evident over the cathodic one. Both growing trends agree with those mentioned above, where temperature favors the kinetic reactions, accordingly, increasing the j_0 values for both electrode processes. This behavior has also been reported in the literature [55,56]. Moreover, observing the values in Table 5, the anodic process shows a higher activation resistance compared to the cathodic one.

Fig. 8 shows the dependence of the cathodic and anodic j_0 values with the inverse of the temperature, specifically for 50 % H_2 concentration. This figure, also well-known as the Arrhenius plot, was used to calculate the E_a for the cathodic and anodic processes. Concerning the cathodic and anodic (j_{01}, j_{02}) values, the activation energies were calculated over the three temperatures, obtaining around 100 kJ/mol and 66 kJ/mol, respectively, which agree with those values reported in the literature [57,58].

Performing the same procedure for the other H_2 concentrations, the obtained E_a values were reported in Fig. 9. Mean value (μ) and standard deviation (σ) were calculated to obtain the coefficient of variation CV (Eq. (14), and its value is around 3 %, and this means that the mean value suitably represents E_a of the whole anodic process:

$$CV \frac{\sigma}{\mu} \quad (14)$$

4. Conclusions

This work presents and discusses SOFC modelling integrated with the experimental activity. I-V curves were obtained at three temperatures (650, 700, and 750 °C) and different H_2 concentrations (15, 25, 50, 75, and 90 %). A summary of the main conclusions and a description in detail are reported below:

- It was performed a 0D-fitting procedure, by using low- and high-voltage Butler Volmer approximations, to determine all the electrochemical parameters related to different physical phenomena associated with an assembled SOFC button cell.
- EIS and DRT have been performed to validate the obtained fitting results and to study in detail the physical phenomena.
- Considering dimensionless charge transfer coefficients of RDS, possible anodic and cathodic reaction mechanisms have been proposed based on the best fitting obtained.

From the experimental data, a fitting process was developed to obtain four parameters (P_0, P_1, P_2, and P_3) representing different physical phenomena associated with the cell. The numerical values for the fitting parameters at different temperatures and hydrogen concentrations are consistent with the expected phenomena trend: P_1 (ohmic

electrolyte resistance parameter) and P_2 (reaction mechanisms parameter) are constant with the H_2 content but vary with temperature, while P_0 (activation polarization resistance) and P_3 (reaction mechanisms and electrode kinetics parameter) change with both temperature and hydrogen concentrations. The model is validated by EIS analysis results. P_0, which amounts to 1.783 $\Omega \cdot cm^2$, falls within the range observed in EIS: 0.26 $\Omega \cdot cm^2$ in OCV and 3 $\Omega \cdot cm^2$ in underload condition of 0.5 A/cm^2. Similarly, the P_1 value equals 0.216 $\Omega \cdot cm^2$ which concurs with the mean value of 0.2 $\Omega \cdot cm^2$ for both OCV and underload conditions.

Moreover, DRT analysis, performed using the EIS measurements, showed the characteristic times associated with anodic and cathodic processes in OCV and at 0.5 A/cm^2. In particular, in OCV conditions, increasing the hydrogen concentration, the mass transport phenomenon related to the gas diffusion process changes, showing a slight shift toward high frequencies; instead, the other phenomena are negligible. In underload conditions, anodic and cathodic polarization losses decrease, and peaks also shift towards higher frequencies, suggesting a kinetic improvement.

Finally, dimensionless charge transfer coefficients α_1 and α_2 equal to 3.5 and 2, respectively, calculated by the most likely anodic and cathodic reaction mechanisms reported in the literature, have been validated through the P_2 parameter obtained by model fitting.

Then, determination of the exchange current densities for both electrodes varying temperature and hydrogen concentration was performed, ranging from 0.024 A/cm^2 to 0.048 A/cm^2 for O_2 reduction and from 0.012 A/cm^2 to 0.073 A/cm^2 for H_2 oxidation, and subsequently the cathodic and anodic Ea, equal to 100 kJ/mol and 66 kJ/mol, respectively has been determined in accordance with the results reported in the literature.

The author's perspective is focused on performing, through the same fitting procedure, a study of different types of SOFC button cells in order to compare and highlight the possible differences between manufacturing designs and suggest possible changes to improve the electrochemical performance.

CRediT authorship contribution statement

Luca Del Zotto: Conceptualization, Methodology, Data curation, Validation, Writing – original draft. **Giacomo Tamburrano:** Methodology, Writing – review & editing. **Alessandro Dell'Era:** Conceptualization, Data curation, Supervision, Writing – original draft, Resources. **Arda Hatunoglu:** Writing – review & editing. **Erwin Ciro:** Methodology, Data curation, Writing – review & editing, Resources.

Declaration of competing interest

The authors declare that they have no known competing financial interests or personal relationships that could have appeared to influence the work reported in this paper.

Data availability

The data that has been used is confidential.

Acknowledgment

The authors acknowledge the funding from the European Union's Horizon 2020 research and innovation program under grant agreement No. 101006656 GICO project and from Lazio Innova S.p.A Progetti di gruppi di ricerca 2020 No. A0375-2020-36678 Zephyrus project.

References

[1] Badal FR, Das P, Sarker SK, Das SK. A survey on control issues in renewable energy integration and microgrid. Prot Control Mod Power Syst 2019;4:8. https://doi.org/10.1186/s41601-019-0122-8.
[2] Shen Y, Yao W, Wen J, He H, Jiang L. Resilient wide-area damping control using GrHDP to tolerate communication failures. IEEE Trans Smart Grid 2019;10:2547–57. https://doi.org/10.1109/TSG.2018.2803822.
[3] Peng X, Yao W, Yan C, Wen J, Cheng S. Two-stage variable proportion coefficient based frequency support of grid-connected DFIG-WTs. IEEE Trans Power Syst 2020;35:962–74. https://doi.org/10.1109/TPWRS.2019.2943520.
[4] Ayyarao TSLV. Modified vector controlled DFIG wind energy system based on barrier function adaptive sliding mode control. Prot Control Mod Power Syst 2019;4:4. https://doi.org/10.1186/s41601-019-0119-3.
[5] Wang Q, Yao W, Fang J, Ai X, Wen J, Yang X, et al. Dynamic modeling and small signal stability analysis of distributed photovoltaic grid-connected system with large scale of panel level DC optimizers. Appl Energy 2020;259:114132. https://doi.org/10.1016/j.apenergy.2019.114132.
[6] Liu J, Yao W, Wen J, Fang J, Jiang L, He H, et al. Impact of power grid strength and PLL parameters on stability of grid-connected DFIG wind farm. IEEE Trans Sustain Energy 2020;11:545–57. https://doi.org/10.1109/TSTE.2019.2897596.
[7] Chaibi Y, Allouhi A, Salhi M, El-jouni A. Annual performance analysis of different maximum power point tracking techniques used in photovoltaic systems. Prot Control Mod Power Syst 2019;4:15. https://doi.org/10.1186/s41601-019-0129-1.
[8] Arteconi A, Del Zotto L, Tascioni R, Cioccolanti L. Modelling system integration of a micro solar Organic Rankine Cycle plant into a residential building. Appl Energy 2019;251:113408. https://doi.org/10.1016/j.apenergy.2019.113408.
[9] Undertaking F-JFC& HJ. Hydrogen Roadmap Europe; 2019. doi: 10.2843/249013.
[10] Bourne S. The future of fuel: the future of hydrogen. Fuel Cells Bull 2012;2012:12–5. https://doi.org/10.1016/S1464-2859(12)70027-5.
[11] Dincer I, Rosen MA. Exergy analysis of fuel cell systems. Exergy energy environ. Sustain Dev 2013:363–82. https://doi.org/10.1016/C2010-0-68369-6.
[12] Staffell I, Scamman D, Velazquez Abad A, Balcombe P, Dodds PE, Ekins P, et al. The role of hydrogen and fuel cells in the global energy system. Energy Environ Sci 2019;12:463–91. https://doi.org/10.1039/C8EE01157E.
[13] McPhail SJ, Conti B, Kiviaho J. The yellow pages of SOFC technology—international status of SOFC deployment. Finland: Espoo; 2017.
[14] Melideo D, Ortiz-Cebolla R, Weidner E. Life cycle assessment of hydrogen and fuel cell technologies; 2020.
[15] Barbir F. Fuel cell applications. PEM fuel cells, Elsevier; 2013. p. 373–434. doi: 10.1016/B978-0-12-387710-9.00010-2.
[16] Felseghi R-A, Carcadea E, Raboaca MS, Trufin CN, Filote C. Hydrogen fuel cell technology for the sustainable future of stationary applications. Energies 2019;12:4593. https://doi.org/10.3390/en12234593.
[17] Marcantonio V, Del Zotto L, Pieter J, Bocci E. Main issues of the impact of tar, H2S, HCl and alkali metal from biomass-gasification derived syngas on the SOFC anode and the related gas cleaning technologies for feeding a SOFC system: a review. Int J Hydrogen Energy 2021;47:517–39. https://doi.org/10.1016/j.ijhydene.2021.10.023.
[18] Ciro E, Dell'Era A, Hatunoglu A, Bocci E, Del Zotto L. Kinetic and thermodynamic study of the wet desulfurization reaction of ZnO sorbents at high temperatures. Energies 2023;16. https://doi.org/10.3390/en16020792.
[19] Fong KF, Lee CK. System analysis and appraisal of SOFC-primed micro cogeneration for residential application in subtropical region. Energy Build 2016;128:819–26. https://doi.org/10.1016/j.enbuild.2016.07.060.
[20] Barelli L, Bidini G, Ottaviano A. Integration of SOFC/GT hybrid systems in microgrids. Energy 2017;118:716–28. https://doi.org/10.1016/j.energy.2016.10.100.
[21] Yang B, Wang J, Zhang M, Shu H, Yu T, Zhang X, et al. A state-of-the-art survey of solid oxide fuel cell parameter identification: modelling, methodology, and perspectives. Energy Convers Manag 2020;213:112856. https://doi.org/10.1016/j.enconman.2020.112856.
[22] Wang R, Lu Y, Ma Y, Sun Z, Gopalan S, Basu SN, et al. Experimental validation of solid oxide fuel cell polarization modeling: an LSM-YSZ/YSZ/Ni-YSZ case study. Electrochim Acta 2020:361. https://doi.org/10.1016/j.electacta.2020.137052.
[23] Bianchi FR, Spotorno R, Piccardo P, Bosio B. Solid oxide fuel cell performance analysis through local modelling. Catalysts 2020:10. https://doi.org/10.3390/catal10050519.
[24] Sahli Y, Zitouni B, Ben-Moussa H. Solid oxide fuel cell thermodynamic study. Çankaya Univ J Sci Eng 2017;14:134–51.
[25] Kuboyama H. Impedance spectra of solid oxide fuel cell. ECS Proc. Vol. 1997;1997-40:404–10. doi: 10.1149/199740.0404pv.
[26] Almutairi G. A simple model for solid oxide fuel cells. Energy Transitions 2020;4:163–7. https://doi.org/10.1007/s41825-020-00031-0.
[27] Costamagna P, Selimovic A, Del Borghi M, Agnew G. Electrochemical model of the integrated planar solid oxide fuel cell (IP-SOFC). Chem Eng J 2004;102:61–9. https://doi.org/10.1016/j.cej.2004.02.005.
[28] Akkaya AV. Electrochemical model for performance analysis of a tubular SOFC. Int J Energy Res 2007;31:79–98. https://doi.org/10.1002/er.1238.
[29] Di Giuseppe G, Licon GM. A modeling study of the effect of cathode delamination on SOFC performance. In: ASME 2008 6th Int. Conf. Fuel Cell Sci. Eng. Technol., ASMEDC; 2008. p. 133–42. doi: 10.1115/FuelCell2008-65030.
[30] Zouhri K, Lee S-Y. Exergy study on the effect of material parameters and operating conditions on the anode diffusion polarization of the SOFC. Int J Energy Environ Eng 2016;7:211–24. https://doi.org/10.1007/s40095-015-0201-1.
[31] Daneshvar K, Dotelli G, Cristiani C, Pelosato R, Santarelli M. Modeling and parametric study of a single solid oxide fuel cell by finite element method. Fuel Cells 2014;14:189–99. https://doi.org/10.1002/fuce.201300235.
[32] Nakajo A, Tanasini P, Diethelm S, Van Herle J, Favrat D. Electrochemical model of solid oxide fuel cell for simulation at the stack scale II: implementation of degradation processes. J Electrochem Soc 2011;158:B1102. https://doi.org/10.1149/1.3596435.

[33] Padinjarethil AK, Bianchi FR, Bosio B, Hagen A. Electrochemical characterization and modelling of anode and electrolyte supported solid oxide fuel cells. Front Energy Res 2021:9. https://doi.org/10.3389/fenrg.2021.668964.
[34] Wang X, Wang FH. Studies of half-cell for anode supported SOFC after reduction. Adv Mater Res 2011;287–290:2511–5. https://doi.org/10.4028/www.scientific.net/AMR.287-290.2511.
[35] Adler SB. Reference electrode placement in thin solid electrolytes. J Electrochem Soc 2002;149:E166. https://doi.org/10.1149/1.1467368.
[36] Gamalath KAILW, Peiris BMP. Theoretical approach to the physics of fuel cells. Int Lett Chem Phys Astron 2012;2:15–27.
[37] Yahya A, Ferrero D, Dhahri H, Leone P, Slimi K, Santarelli M. Electrochemical performance of solid oxide fuel cell: experimental study and calibrated model. Energy 2018;142:932–43. https://doi.org/10.1016/j.energy.2017.10.088.
[38] Subotić V, Königshofer B, Juričić Đ, Kusnezoff M, Schröttner H, Hochenauer C, et al. Detailed insight into processes of reversible solid oxide cells and stacks using DRT analysis. Energy Convers Manag 2020:226. https://doi.org/10.1016/j.enconman.2020.113509.
[39] Alboghobeish M, Ferrario AM, Pumiglia D, Della Pietra M, McPhail SJ, Pylypko S, et al. Developing an automated tool for quantitative analysis of the deconvoluted electrochemical impedance response of a solid oxide fuel cell. Energies 2022:15. https://doi.org/10.3390/en15103702.
[40] Schichlein H, Müller AC, Voigts M, Krügel A, Ivers-Tiffée E. Deconvolution of electrochemical impedance spectra for the identification of electrode reaction mechanisms in solid oxide fuel cells. J Appl Electrochem 2002;32:875–82. https://doi.org/10.1023/A:1020599525160.
[41] Ivers-Tiffée E, Weber A. Evaluation of electrochemical impedance spectra by the distribution of relaxation times. J Ceram Soc Jpn 2017;125:193–201. https://doi.org/10.2109/jcersj2.16267.
[42] Leonide A, Sonn V, Weber A, Ivers-Tiffée E. Evaluation and modeling of the cell resistance in anode-supported solid oxide fuel cells. J Electrochem Soc 2008;155:B36. https://doi.org/10.1149/1.2801372.
[43] Caliandro P, Nakajo A, Diethelm S, Van herle J. Model-assisted identification of solid oxide cell elementary processes by electrochemical impedance spectroscopy measurements. J Power Sources 2019;436:226838. https://doi.org/10.1016/j.jpowsour.2019.226838.
[44] Del Zotto L, Monforti Ferrario A, Hatunoglu A, Dell'era A, McPhail S, Bocci E. Experimental procedures & first results of an innovative solid oxide fuel cell test rig: parametric analysis and stability test. Energies 2021;14:1–19. https://doi.org/10.3390/en14082038.
[45] Wan TH, Saccoccio M, Chen C, Ciucci F. Influence of the discretization methods on the distribution of relaxation times deconvolution: implementing radial basis functions with DRTtools. Electrochim Acta 2015;184:483–99. https://doi.org/10.1016/j.electacta.2015.09.097.
[46] Schlüter N, Ernst S, Schröder U. Finding the optimal regularization parameter in distribution of relaxation times analysis. ChemElectroChem 2019;6:6027–37. https://doi.org/10.1002/celc.201901863.
[47] Marcelo D, Dell'Era A. Economical electrolyser solution. Int J Hydrogen Energy 2008;33:3041–4. https://doi.org/10.1016/j.ijhydene.2008.02.078.
[48] Li H, Wei W, Liu F, Xu X, Li Z, Liu Z. Identification of internal polarization dynamics for solid oxide fuel cells investigated by electrochemical impedance spectroscopy and distribution of relaxation times. Energy 2023;267:126482. https://doi.org/10.1016/j.energy.2022.126482.
[49] Bessler WG, Warnatz J, Goodwin DG. The influence of equilibrium potential on the hydrogen oxidation kinetics of SOFC anodes. Solid State Ion 2007;177:3371–83. https://doi.org/10.1016/j.ssi.2006.10.020.
[50] Bessler WG, Vogler M, Störmer H, Gerthsen D, Utz A, Weber A, et al. Model anodes and anode models for understanding the mechanism of hydrogen oxidation in solid oxide fuel cells. Phys Chem Chem Phys 2010;12:13888–903. https://doi.org/10.1039/c0cp00541j.
[51] Li Y, Gemmen R, Liu X. Oxygen reduction and transportation mechanisms in solid oxide fuel cell cathodes. J Power Sources 2010;195:3345–58. https://doi.org/10.1016/j.jpowsour.2009.12.062.
[52] Gong M, Gemmen RS, Liu X. Modeling of oxygen reduction mechanism for 3PB and 2PB pathways at solid oxide fuel cell cathode from multi-step charge transfer. J Power Sources 2012;201:204–18. https://doi.org/10.1016/j.jpowsour.2011.11.002.
[53] Guidelli R, Compton RG, Feliu JM, Gileadi E, Lipkowski J, Schmickler W, et al. Defining the transfer coefficient in electrochemistry: an assessment (IUPAC Technical Report). Pure Appl Chem 2014;86:245–58. https://doi.org/10.1515/pac-2014-5026.
[54] Bockris JO, Nagy Z. Simmetry factor and trasnfer coefficient. J Chern Ed 1973;50:839–43.
[55] Fukumoto T, Endo N, Natsukoshi K, Tachikawa Y, Harrington GF, Lyth SM, et al. Exchange current density of reversible solid oxide cell electrodes. Int J Hydrogen Energy 2022;47:16626–39. https://doi.org/10.1016/j.ijhydene.2022.03.164.
[56] Yonekura T, Yachikawa Y, Yoshizuma T, Shiratori Y, Ito K, Sasaki K. Cathode electrolyte anode. ECS Trans 2011;35:1007–14.
[57] Marina OA, Pederson LR, Williams MC, Coffey GW, Meinhardt KD, Nguyen CD, et al. Electrode performance in reversible solid oxide fuel cells. J Elec Soc 2007;154:B452. https://doi.org/10.1149/1.2710209.
[58] Zhang X, Wang L, Espinoza M, Li T, Andersson M. Numerical simulation of solid oxide fuel cells comparing different electrochemical kinetics. Int J Energy Res 2021;45:12980–95. https://doi.org/10.1002/er.6628.